ACS APPLIED MATERIALS & INTERFACES

Research Article

www.acsami.org

Pt@Au Nanorods Uniformly Decorated on Pyridyne Cycloaddition Graphene as a Highly Effective Electrocatalyst for Oxygen Reduction

Xing Zhong, Huiyou Yu, Xinde Wang, Lin Liu, Yu Jiang, Lei Wang, Guilin Zhuang, Youqun Chu, Xiaonian Li, and Jian-guo Wang*

College of Chemical Engineering, Zhejiang University of Technology, Hangzhou 310014, China

Supporting Information

ABSTRACT: Preparing metal-supported graphene nanocomposites is both interesting and challenging because of their well-defined morphologies and have potential application for oxygen reduction reaction (ORR). Here, we present an easy approach to synthesizing a novel hybrid material composed of Pt@Au nanorods (NRs) uniformly dispersed on the pyridyne cycloaddition of graphene (Pt@Au-PyNG), and the material serves as a high-performance catalyst for ORR. This hybrid electrocatalyst significantly decreases the use of Pt by using Pt dispersed on Au NRs and shows a markedly high activity toward ORR. The resulting Pt@Au-PyNG hybrid displayed comparable electrocatalytic activity and better stability than commercial Pt/C in alkaline solutions toward ORR. The hybrid effectively blocks CO formation to increase catalyst resistance to CO poisoning, thereby decreasing the amount of Pt needed. Free-energy diagrams for ORR on Pt@Au (111) through dissociative and associative mechanisms show that OH or O hydrogenation is the rate-limiting step based on DFT calculations.

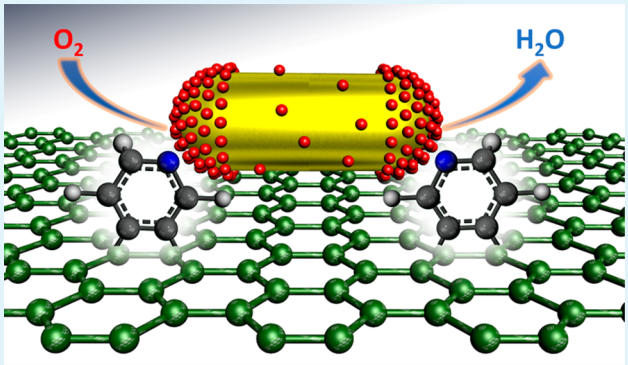

KEYWORDS: *pyridyne, platinum, gold, graphene, electrocatalysts, oxygen reduction*

INTRODUCTION

Given the growing demand for alternative energy worldwide, polymer electrolyte membrane fuel cells (PEMFCs) are recognized as one of the most important technologies for sustainable development in our future.[1−3] Pt is well-known as an efficient catalyst in PEMFCs, and Pt-based electrocatalysts are considered to have promising practical applications.[4] However, a major limiting factor is that the sluggish kinetics of the oxygen reduction reaction (ORR) requires a substantial amount of Pt, which hampers its commercial adoption. Thus, exploring new strategies to reduce Pt usage while minimizing loss of the ORR catalytic efficiency is important.

Various Pt-based electrocatalysts were developed to address the aforementioned challenges. The innovations include alloying Pt with nonprecious metals, including Fe, Co, Ni, Cu, and Mn, and this process is demonstrated as a successful approach to enhancing ORR kinetics.[5−9] However, obtaining Pt alloy nanoparticles with definite composition distribution or ordered intermetallic phases is difficult. Another effective approach is Pt-loaded onto nanomaterials as supported catalysts. Graphene-based materials have been proven to be ideal candidates for catalyst support. They have not only a large specific surface area that decrease the aggregation of the electrocatalysts, but also good conductivity enable better electron transfer.[10,11] In addition, various graphene-metal oxide (sulfide) hybrids were also developed and successfully used in fuel cells.[12−15] However, controlling the synthesis of graphene-metal oxide (sulfide) hybrids prepared by in situ growth is limited by the solution reaction based on metal precursors and graphene. Metal-based catalysts assembly on graphene surface has been proven as an alternative way cause of the desired morphology of nanoparticles can be easily obtained and controlled. Sun et al. deposit highly dispersed preprepared PtFe or Co−CoO nanoparticles onto graphene by using an easy, self-assembly method.[16,17] Nevertheless, very limited successful examples have been reported in developing a controllable assembly of metals on graphene because of the weak interaction between metal nanoparticles and graphene.

Thus, preparing metal-supported graphene nanocomposites is interesting and challenging because of their well-defined morphologies and potential use as effective electrocatalysts for ORR. In this regard, we have systematically investigated the role of carbon vacancy[18] doped-B, N,[19] surface-adsorbed oxygen-containing species in stabilizing Pt, Au, and Pd on carbon materials.[20] Our group has also proved that the pyridyne cycloaddition of graphene (PyNG) can provide "external" pyridine-N as active sites for ORR.[21] The "external" pyridine-N can probably act as the anchoring site for metal nanoparticles and exert a synergetic coupling effect between pyridine-N doped graphene and Pt nanoparticles. It can also

Received: April 6, 2014
Accepted: August 7, 2014
Published: August 7, 2014

   dx.doi.org/10.1021/am5020452 | ACS Appl. Mater. Interfaces 2014, 6, 13448−13454

possibly lower the dissociation activation energy of molecular O_2, and sequentially enhance electrocatalytic activity. Meanwhile, Au nanorods (NRs) are attracting increasing attention because of their unique properties and potential applications, such as in biomedical sensors, plasmon-enhanced spectroscopies, and optical devices.[22−25] However, studies rarely focus on Au NRs as synergistic catalysts.[26−28] The incorporation of Au can suppress Pt dissolution and migration of CO poisoning, resulting in better activities during ORR.[29−31] In the present study, we establish an easy approach to obtained Pt@Au NRs uniformly dispersed on PyNG (Pt@Au-PyNG) as a novel hybrid electrocatalyst for ORR. This hybrid electrocatalyst significantly decreases the use of Pt through Pt dispersed on Au NRs and shows markedly high activity toward ORR. Compared with Pt/C, the resulting Pt@Au-PyNG hybrid displayed comparable electrocatalytic activity and better stability than commercial Pt/C in alkaline solutions toward ORR. It can effectively block CO formation that increases the catalyst's resistance, thereby markedly decreasing the amount of Pt needed. DFT calculations are performed to describe the free-energy landscape of the electrochemical ORR reaction over Pt@Au as a function of applied bias. The possible reaction mechanism is discussed on the basis of a free-energy diagram.

EXPERIMENTAL SECTION

Materials. Graphene Nanopowder (98%) were purchased from Graphene Supermarket (Graphene Laboratories Inc.). Cesium fluoride (99%) and acetonitrile (99.9%) were purchased from J&K Scientific Ltd. Commercial 20 wt % Pt/C were purchased from Alfa Aesar. Hexadecyltrimethylammonium bromide (CTAB, >98.0%) and 5-bromosalicylic acid (>98.0%) were purchased from J&K Scientific Ltd. Tetrachloroauric acid ($HAuCl_4{\cdot}3H_2O$), sodium borohydride ($NaBH_4$, 99%), silver nitrate ($AgNO_3$, >99%), and L-ascorbic acid (≥99%) were purchased from Sigma-Aldrich. 18.2 MΩ Milli-Q water was used through the whole experiment and all solvents were obtained from commercial suppliers and used without further purification.

Materials Synthesis. The Pt@Au-PyNG hybrid was fabricated as shown in Scheme 1. Monodispersed Au NRs were prepared using the seed-mediated growth method.[32] Pt deposited on Au NRs were prepared according to literature with some modification.[33,34] The PyNG was prepared according to our previously reported method.[21] For comparing, the Pt@Au NRs/pristine graphene (Pt@Au-PG) was also prepared by the similar method as Pt@Au-PyNG, whereas the PG was replace of the PyNG.

Scheme 1. Schematic Representation of the Pt@Au-PyNG Hybrid

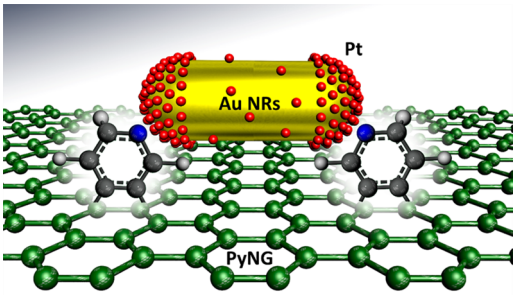

Pyridyne precursors and PyNG were prepared according to our previously reported procedures.[21]

Synthesis of Au NRs. The Au NRs seed solution was prepared with a little modification as reported previously.[32,35] A 5 mL (0.2 M) CTAB solution and 5 mL (0.5 mM) $HAuCl_4$ solution were mixed together; 1 mL (0.01 M) of $NaBH_4$ was then injected into the above-mentioned solution. We observed that the solution color changed to brownish-yellow. The solution was aged for 60 min before use for next procedure.

The growth solution was prepared by using 9.0 g of CTAB and 1.1 g of 5-Bromosalicylic acid dissolved in 250 mL of water in a 500 mL Erlenmeyer flask, and 12 mL (4 mM) of $AgNO_3$ solution was then added. Let the mixture stand for 30 min at room temperature, after which 250 mL (1 mM) of $HAuCl_4$ solution was added. The solution was slowly stirred for 15 min, and then 2 mL (0.064 M) of ascorbic acid was added. At this time, the solution became transparent. At last, 0.8 mL of as-prepared fresh seed solution was injected. The obtained mixture was stirred for 60 s and left standing for 12 h with the purpose of Au NRs growth. After complete the reaction, the as-prepared Au NRs solution were used for next step without post-treatment. The products were obtained by centrifugation at 9000 rpm for half an hour, and the products were redispersed in 5 mL of water.

Synthesis of Pt@Au NRs. Platinum growth was carried out in the presence of Ag^+ ions, because although Ag^+ ions were present in the solution, Pt preferentially deposited on the rod tips of Au nanorods.[34] Five milliliters (0.48 mM) of Au NRs were redispersed in 10 mL (0.1 M) of CTAB; 395 μL (2 mM) of K_2PtCl_4 was added to 5 mL (0.157 mM) of Au NRs at 40 °C and left for 30 min, and then 157 μL (0.1 M) of ascorbic acid was added. The solution was maintained at 40 °C overnight. Finally, the Pt-coated Au NRs were obtained by centrifugation at 9000 rpm for 30 min, then redispersed in ethanol.

Synthesis of Pt@Au-PyNG. As-prepared Pt@Au NRs were centrifuged and concentrated, then dispersed in 5 mL of DMF, 5 mg of PyNG was added, the flask was sonicated for 30 min, and then the dispersion was stirring overnight. After completion of the reaction, the Pt@Au-PyNG was separated from the mixture by centrifugation, washed with DMF and ethanol thoroughly, then the product was collected by filtration and dried in vacuo overnight. For the purpose of comparsion, in the similar way, the Pt@Au-PG was also prepared by using PG instead of PyNG.

Characterization Methods. Transmission electron microscopy (TEM) images were performed on Tecnai G2F30S-Twin electron microscope operating at 300 kV. X-ray photoelectron spectroscopy (XPS) analysis was carried on Kratos AXIS Ultra DLD X-ray photoelectron spectrometer. The optical characterization was carried out by UV−vis-NIR spectroscopy with U-4100 spectrophotometer. XRD data was obtained by a XPERT-PRO X-ray diffractmeter using Cu K αradiation. Scanning electron microscopy (SEM) images were performed on JSM-6701F. Cyclic voltammetry (CV) experiments were performed on CHI660D electrochemical analyzer (CHI Instrument Corp. Shanghai). Rotating disk electrode (RDE) measurements were performed on CHI 760C and MSR electrode rotator from Pine Research Instrumentation.

Electrochemical Measurements. Five milligrams of the samples were dispersed in a solution containing 0.2 mL of 5 wt % Nafion aqueous solution and 4.8 mL of deionized water (1 $mg.mL^{-1}$). The mixtures were ultrasonicated for 10 min to obtain a homogeneous catalyst ink. To prepare the working electrode for electrochemical measurements, 10 μL of the above-mentioned suspension was dipped on a glass carbon electrode (4 mm in diameter). For comparison, 1 mg mL^{-1} commercially 20 wt % Pt/C was also used, 5 μL of the 20 wt % Pt/C ink was dipped on a glass carbon electrode (4 mm in diameter).

Cyclic voltammetry (CV) experiments: the working electrode was inserted into the cell setup, which is composed of an Ag/AgCl/KCl (3 M) reference electrode, a Pt counter electrode, and a 30 mL glass cell containing 20 mL of 0.1 M KOH aqueous electrolyte. Before test, electrolyte was saturated with O_2. In order to ensure O_2 saturation during the recording of CVs, a flow of O_2 was maintained over the electrolyte. The RDE linear voltammetry was performed from −1.0 and +0.2 V at different scan rate of 100 mV s^{-1}.

Rotating disk electrode (RDE) measurement: An Ag/AgCl/KCl (3 M) and a Pt sheet were used as reference and the counter electrodes, respectively. And the same amount of the catalyst as CV used was dipped on a rotating glass carbon electrode (3 mm in diameter). The linear sweep voltammograms with a scan rate of 10 mV s^{-1} at rotating

speeds range from 400 to 2025 rpm were recorded in O_2 saturated 0.1 M KOH.

Kinetics analysis: According to Koutecky–Levich equation

$$\frac{1}{j} = \frac{1}{j_k} + \frac{1}{B\omega^{1/2}}$$

Where j is the current, ω is the electrode rotating speed in rpm, j_k is the kinetic current, and B is the Levich slope, which was determined as follows

$$B = 0.2nFC_0(D_0)^{2/3}\nu^{-1/6}$$

Where the constant 0.2 is adopted when the rotating speed is in rpm, n is the number of electrons transferred per mole of O_2, D_0 is the diffusion coefficient of O_2 in 0.1 M KOH ($1.9 \times 10-5$ cm s^{-1}), C_0 is the concentration of O_2 (1.2×10^{-3} mol L^{-1}), F is the Faraday constant (96485 C mol^{-1}), and ν is the kinetic viscosity (0.01 cm^2 s^{-1}).

Computational Section. All the DFT calculations were carried out using the Vienna ab initio simulation package (VASP)[36−38] code with projector augmented wave (PAW) potentials. To simulate Pt@Au NRs, four layers (3×3) Au (111) was used, in which one row Au are substituted by Pt in each layer (Pt@Au (111)). The adsorption of possible reaction intermediates (O, OH, and OOH) were investigated. The vacuum layer is 15 Å between the repeating slab. During the geometry optimizations, only two bottom layers were fixed. The Brillouin zone integration was performed using the Monkhorst–Pack scheme with $4 \times 4 \times 1$. The convergence criterion of the force and energy is 10 meV/ Å and 0.01 meV, respectively. The free energies of various intermediates were calculated at 300 K and 1 bar based on approach proposed by Norskov.[39] The entropic corrections and zero-point energy (ZPE) have been included into the free energies of all intermediates.

RESULTS AND DISCUSSION

Scanning electron microscopy (SEM) and transmission electron microscopy (TEM) were used to investigate the morphology of PG, Au NRs, and Pt@Au-PyNG (Figure 1 and Figure S1–S3 in the Supporting Information). PG displays a voile-like structure and average flake thickness of PG was less than 3 monolayers, as shown in Figure S1 in the Supporting Information. Au NRs have an average length of 50 nm and an average width of 20 nm, which indicated that the aspect ratio was 2.5 ± 0.5. It is noteworthy that a majority of Pt were deposited at the ends of the Au NRs when Pt is added. High-angle annular dark-field scanning TEM (HAADF-STEM) images of Pt@Au NRs are presented in Figure 1. The EDX elemental mapping images reveal that the Pt@Au NRs have greater Pt concentration at the ends of Au NRs. The tendency of Pt's preferential growth at the ends of Au NRs is due to the platinum deposition in the presence of Ag^+.[33,34] As shown in Figure S2 in the Supporting Information, unsupported Au NRs and Pt@Au NRs easily agglomerate. When Au NRs or Pt@Au NRs adsorb onto PyNG, very limited aggregation phenomena are observed. The SEM images (Figure S3) also confirm that Pt@Au NRs are uniformly dispersed on PyNG, which indicate that the strong coupling effect between Au NRs and pyridine-N in PyNG can obviously decrease agglomeration. Consequently, electrocatalytic performance is positively influenced.

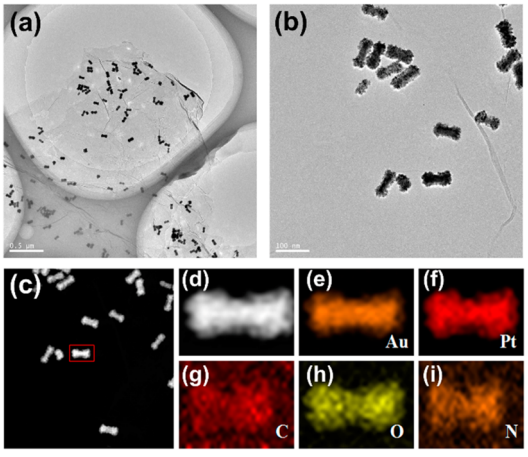

Figure 1. (a) TEM image of Pt@Au-PyNG with a scale bar of 0.5 μm. (b) TEM image of Pt@Au-PyNG with a scale bar of 100 nm. (c) HAADF-STEM image of Pt@Au-PyNG. (d-i) EDX maps of Pt@Au-PyNG, Au, Pt, C, O, and N, respectively.

The UV–vis absorption spectra of the samples is shown in Figure 2a. Au NRs exhibit two distinct absorption bands at 525 and 705 nm corresponding to transverse and longitudinal (LSPR) plasmon resonance absorption, respectively.[22] When Pt is deposited onto Au NRs, the LSPR peak is red-shifted and broadened, which well agrees with previous observations on the deposition of Pt onto Au NRs. After coating Pt@Au NRs on PyNG, the absorption bands of Pt@Au NRs almost disappear. This change can be attributed to the tight coupling effects between PyNG and Pt@Au NRs. We also observed that the peaks around 400–450 nm in three samples, we speculated that the peaks may origin from the very little of silver residuals throughout the synthetic process. Figure 2b displays the XRD patterns of PyNG, Au-PyNG and Pt@Au-PyNG. For PyNG, a broad peak at 25° is observed. This peak is the (002) diffraction from graphene and can be attributed to the regular stacking of PG destroyed by the pyridyne cycloaddition. For Au-PyNG, the peaks at 38.1, 44.3, 65.6, 77.6, and 81.8° are clearly recognized and correspond to the (111), (200), (220), (311), and (222) diffraction planes of Au. The Pt@Au-PyNG shows the similar peaks with Au-PyNG, the reason is that the patterns of Pt were almost overlapped with Au. The XRD patterns of Pt and Au are in good agreement with Pt (JCPDS 04–0802) and Au (JCPDS 04–0784), confirming that the as-synthesized Pt@Au-PyNG have a good crystallization resulting from ordered structures as previously observed.[40−42] XRD demonstrates that Pt@Au NRs are successfully deposited onto PyNG. The compositions of Pt@Au-PyNG was also determined by X-ray photoelectron spectroscopy (XPS). The high-resolution C 1s XPS spectrum of Pt@Au PyNG (see Figure S4 in the Supporting Information) can be fitted into three peaks centered at 284.5, 285.3, and 286.4 eV, corresponding to C═C, C═N, and C–OH. The "external" pyridinic-N peak was located at 399.5 eV, which is consistent with our previous report results.[21] The XPS spectra of the Pt 4f and Au 4f regions are also depicted in Figure 2c, d. The binding energies of Pt 4f ($4f_{7/2}$ = 71.1 eV, $4f_{5/2}$ = 74.4 eV) and Au 4f ($4f_{7/2}$ = 84.1 eV, $4f_{5/2}$ = 87.8 eV) peaks are observed, indicating that Pt and Au exist in the form of Pt^0 and Au^0 atoms. The element contents were determined on the basis of the XPS analysis and are displayed in Table S1 in the Supporting Information. As expected, 2.61 at % Pt is found in Pt@Au-PyNG. However, Pt shows strong signals, whereas the intensity of Au is only slightly detected. This phenomenon is mainly due to the deposition of Pt onto Au NRs that leads to the formation of a Pt shell on Au NRs. The results are similar to those of other studies.[43]

We further evaluated the PG, PyNG, Au-PyNG, Pt@Au-PG, and Pt@Au-PyNG by using cyclic voltammetry (CV) (Figure

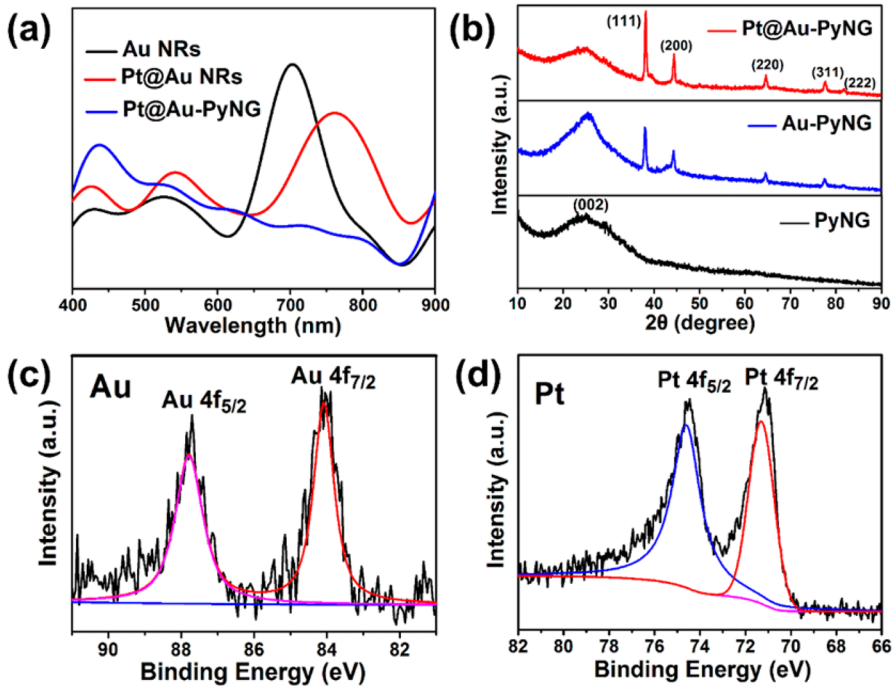

Figure 2. (a) UV−vis spectra of Au NRs, Pt@Au-PG, and Pt@Au-PyNG; (b) XRD patterns of PyNG, Au-PyNG, and Pt@Au-PyNG; (c) Au 4f and (d) Pt 4f XPS survey spectra of Pt@Au-PyNG.

3a) to demonstrate the ORR electrocatalytic activity. Unmodified PG displays slight catalytic activity, whereas PyNG electrodes exhibit a modest cathodic ORR peak at −0.36 V. As expected, Pt@Au-PyNG shows an ORR peak at the most positive potential (−0.05 V) and higher current density (−3.44 mA cm^{-2}) among all electrodes (Figure 3a and Figure S5 in the Supporting Information). The electrocatalytic activities are in the order of Pt@Au-PyNG > Pt@Au-PG > Au-PyNG > PyNG. This result displays the remarkable catalytic performance of Pt@Au-PyNG hybrid for ORR. The reason why the Pt@Au-PyNG hybrid exhibit superior ORR activity can be mainly attributed to two aspects: on the one hand, the small size effects of Pt-activating oxygen molecules; and on the other hand, the combination of Pt@Au NRs and PyNG decreasing the energy barrier of the rate-limiting step of ORR. These results clearly demonstrate that PyNG in the Pt@Au-PyNG hybrid may serve as the support and plays an important role in metal−support interactions.

To gain insight into the ORR mechanism of the Pt@Au-PyNG, we performed linear sweep voltammetry (LSV) measurements (Figure 3b and Figure S6 in the Supporting Information). The Pt@Au-PyNG electrocatalyst with an onset potential of −0.06 V, which was approach to commercial 20 wt % Pt/C (−0.03 V) toward ORR as shown in Figure S6 in the Supporting Information. Moreover, the ORR reaction current of Pt@Au-PyNG is also explicitly higher than those of PG, PyNG, and Pt@Au-PG toward limiting current density, which agrees with the CV results. This finding indicates that the electrocatalytic behavior of Pt@Au-PyNG for ORR is significantly influenced by the strong coupling effects between the Pt@Au NRs and PyNG. Moreover, among these electrocatalysts, the Pt@Au-PyNG have the highest specific and mass activity, we observed a significantly enhanced mass activity of the Pt@Au-PyNG, which was 5-fold higher than that of the commercial 20% Pt/C catalyst for the ORR at −0.8 V (see Figure S7 in the Supporting Information). Considering that the amount of Pt and Au used are much less than conventional 20 wt % Pt/C, the improved Pt utilization is also clearly exemplified by the decorated structure. Thus, we believe that the Pt@Au-PyNG have a comparable electrocatalytic activity with commercial Pt/C toward ORR.

The corresponding Koutecky−Levich plots (J^{-1} vs $\omega^{-1/2}$) were analyzed at an electrode potential of −0.6 V (Figure 3c and Figure S8 in the Supporting Information). The plots of all samples show good linear relationship and the corresponding Koutecky−Levich plots at −0.6 V electrode potential reveal that the Pt@Au-PyNG has high ORR current, which is approaching to that of Pt/C and not surprisingly significantly superior to PG, PyNG, and Pt@Au-PG. The transferred electron number n value of Pt@Au-PyNG is 3.7 (Figure 3d), indicating that four electron transfer pathways primarily occur during ORR on the Pt@Au-PyNG, which benefits the construction of fuel cells with high efficiency. A methanol crossover test on the Pt@Au-PyNG electrocatalyst was also performed by chronoamperometric responses as shown in Figure 3e. After the subsequent methanol addition, the ORR current for the Pt@Au-PyNG and PyNG almost remains unchanged, whereas a slight change occurred for the Pt@Au-PG. As expected, a sharp decrease for Pt/C is detected after methanol injection. This result indicates that the Pt@Au-PyNG not only has the excellent electrocatalytic activity but also has outstanding stability and immunity toward methanol crossover.

Furthermore, the stability of the electrocatalysts is another important aspect that needs considering. It can be clearly seen from Figure 3f that the commercial Pt/C suffered a current loss of 35% after 2000 cycles, whereas the ORR activities for the Pt@Au-PyNG and the Pt@Au-PG exhibit a slightly attenuation with high current retention of 99.1 and 94.5%, respectively. The excellent stability of the Pt@Au-PyNG electrocatalyst demonstrating a strong coupling between the Pt@Au NRs and PyNG.

dx.doi.org/10.1021/am5020452 | ACS Appl. Mater. Interfaces 2014, 6, 13448−13454

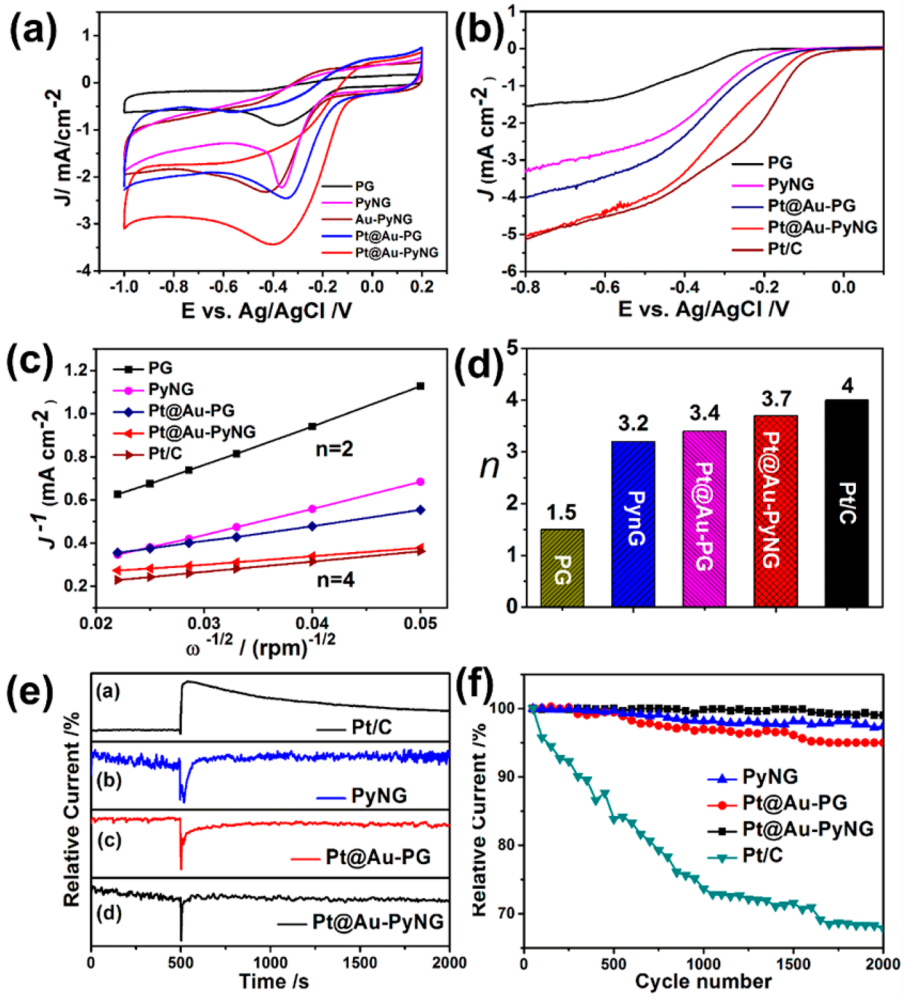

Figure 3. (a) CVs curves of the samples in O_2-saturated 0.1 M KOH; (b) LSV curves of the samples on an RDE (1600 rpm) in an O_2-saturated 0.1 M KOH solution; (c) Koutecky–Levich plots of the samples at −0.6 V; (d) electron transfer numbers of the samples at −0.6 V, respectively; (e) methanol crossover evaluation from the *i*–*t* chronoamperometric response in aqueous solution of KOH (0.1M) saturated with O_2; (f) endurance test of the samples for 2000 cycles in 0.1 M KOH.

The aforementioned results further confirm that Pt@Au NRs coated with PyNG can be an effective strategy with high corrosion resistance and excellent electrocatalytic activity in ORR.

In this study, both dissociative and associative mechanisms are considered. In the former, adsorbed O_2 first dissociates into atomic O, and then the atomic hydrogen is converted into H_2O through two consecutive hydrogenation steps. In the latter mechanism, the adsorbed is hydrogenated into OOH, and then OOH is split into atomic O and OH. These species (O and OH) are then hydrogenated into H_2O. The optimized geometries of the possible reaction intermediates (O_2, O, OH, and OOH) are shown in Figure 4a and Table S2 in the Supporting Information. The most stable adsorption site for all species is Pt. Using the binding energies, the free-energy diagrams for ORR on Pt@Au (111) through dissociative and associative mechanisms are shown in Figure 4b, c. At zero cell potential, all elementary steps in the two reaction mechanisms are strongly exothermic. At the equilibrium potential (1.23 V), the dissociation of O_2 in the dissociative mechanism and OOH in the associative mechanism is downhill, consistent with literature.[44] However, the hydrogenation steps are uphill. For the dissociative mechanism, OH hydrogenation to yield H_2O has the most positive free-energy change. For the associative mechanism, O hydrogenation is slightly more difficult than the OH hydrogenation step. It was found that on Pt (111) surfaces, parallel mechanism (both dissociative and associative) works due to the easily dissociation of O_2 on Pt (111), whereas ORR was difficult occurred due to the weak adsorption of O_2 on Au (111).[44] The addition of Pt on Au (111) (for example Pt@Au (111) or PtAu alloy), the moderate adsorption energy of O_2 and large dissociation energy leads to the easily formation of OOH.[45] For the nitrogen-doped graphene, four electron transfer pathway was proved to be the dominant route for ORR via the OOH reaction intermediate.[21,46,47] Meanwhile, recent theoretical study shows that the defective graphene used as a support may improve the catalytic activity of Pt_{13} nanoparticles for ORR reaction because of the electron transfer effect.[48] Therefore, it is concluded that the synergetic effect of Au and Pt, Pt@Au (111), and PyNG leads to four electron transfer pathway of ORR on Pt@Au-PyNG, which can explain the experimental measurement shown in Figure 3.

CONCLUSION

We successfully designed and prepares a novel Pt@Au-PyNG hybrid through strong coupling effect between Pt@Au NRs and

dx.doi.org/10.1021/am5020452 | ACS Appl. Mater. Interfaces 2014, 6, 13448−13454

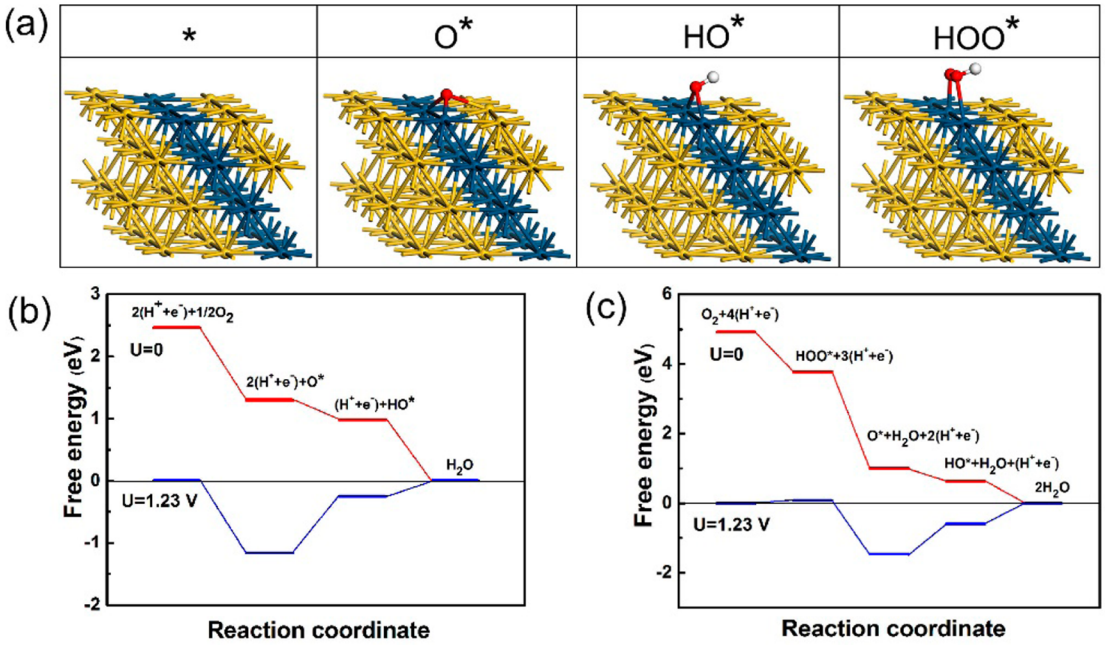

Figure 4. (a) Optimized geometries of Pt@Au (111) and O, OH, and OOH intermediates on Pt@Au (111); free energy diagram for ORR on Pt@Au (111) through (b) dissociative and (c) associative mechanisms, respectively.

PyNG. The Pt@Au-PyNG exhibited excellent electrocatalytic performance, with enhanced electrocatalytic stability and superior methanol tolerance than Pt/C toward ORR. DFT calculations were performed to generate free-energy diagrams for ORR on Pt@Au (111) through dissociative and associative mechanisms. OH or O hydrogenation was determined as the rate-limiting step. This work offered a promising alternative strategy for the next generation of cost-effective Pt-based catalysts in fuel cells and enabled the fabrication of various kinds of metal/graphene nanohybrids with potential applications in catalysts, batteries, and supercapacitors.

■ ASSOCIATED CONTENT

Supporting Information

TEM and SEM of Au NRs, Au-PyNG, Pt@Au NRs, and Pt@Au-PyNG; XPS of Pt@Au-PyNG; LSV and corresponding Koutecky–Levich plot of PyNG, Pt@Au-PG, Pt@Au-PyNG, and Pt/C; and computational calculation details. This material is available free of charge via the Internet at http://pubs.acs.org.

■ AUTHOR INFORMATION

Corresponding Author

*E-mail: jgw@zjut.edu.cn.

Notes

The authors declare no competing financial interest.

■ ACKNOWLEDGMENTS

This work was supported by National Basic Research Pro-gram of China (973 Program) (2013CB733501) and the National Natural Science Foundation of China (NSFC-21306169, 21176221, 21136001, 21101137, and 91334103).

■ REFERENCES

(1) Debe, M. K. Electrocatalyst Approaches and Challenges for Automotive Fuel Cells. *Nature* **2012**, *486*, 43–51.
(2) Tollefson, J. Hydrogen Vehicles: Fuel of the Future? *Nature* **2010**, *464*, 1262–1264.
(3) Demirdoven, N.; Deutch, J. Hybrid Cars Now, Fuel Cell Cars Later. *Science* **2004**, *305*, 974–976.
(4) Wu, J.; Yang, H. Platinum-Based Oxygen Reduction Electrocatalysts. *Acc. Chem. Res.* **2013**, *46*, 1848–1857.
(5) Guo, S.; Zhang, S.; Sun, S. Tuning Nanoparticle Catalysis for The Oxygen Reduction Reaction. *Angew. Chem., Int. Ed.* **2013**, *52*, 8526–8544.
(6) Wang, C.; Markovic, N. M.; Stamenkovic, V. R. Advanced Platinum Alloy Electrocatalysts for the Oxygen Reduction Reaction. *ACS Catal.* **2012**, *2*, 891–898.
(7) Stephens, I. E. L.; Bondarenko, A. S.; Gronbjerg, U.; Rossmeisl, J.; Chorkendorff, I. Understanding the Electrocatalysis of Oxygen Reduction on Platinum and Its Alloys. *Energy Environ. Sci.* **2012**, *5*, 6744–6762.
(8) Choi, S. I.; Lee, S. U.; Kim, W. Y.; Choi, R.; Hong, K.; Nam, K. M.; Han, S. W.; Park, J. T. Composition-Controlled PtCo Alloy Nanocubes with Tuned Electrocatalytic Activity for Oxygen Reduction. *ACS Appl. Mater. Interfaces* **2012**, *4*, 6228–6234.
(9) Wang, M.; Zhang, W. M.; Wang, J. Z.; Wexler, D.; Poynton, S. D.; Slade, R. C. T.; Liu, H. K.; Winther-Jensen, B.; Kerr, R.; Shi, D. Q.; Chen, J. PdNi Hollow Nanoparticles for Improved Electrocatalytic Oxygen Reduction in Alkaline Environments. *ACS Appl. Mater. Interfaces* **2013**, *5*, 12708–12715.
(10) Huang, C.; Li, C.; Shi, G. Graphene Based Catalysts. *Energy Environ. Sci.* **2012**, *5*, 8848–8868.
(11) Wang, D.-W.; Su, D. Heterogeneous Nanocarbon Materials for Oxygen Reduction Reaction. *Energy Environ. Sci.* **2014**, *7*, 576–591.
(12) Zhu, C.; Dong, S. Recent Progress in Graphene-Based Nanomaterials as Advanced Electrocatalysts towards Oxygen Reduction Reaction. *Nanoscale* **2013**, *5*, 1753–1767.
(13) Zhou, X.; Qiao, J.; Yang, L.; Zhang, J. A Review of Graphene-Based Nanostructural Materials for Both Catalyst Supports and Metal-Free Catalysts in PEM Fuel Cell Oxygen Reduction Reactions. *Adv. Energy Mater.* **2014**, DOI: 10.1002/aenm.201301523.
(14) Liang, Y.; Li, Y.; Wang, H.; Dai, H. Strongly Coupled Inorganic/Nanocarbon Hybrid Materials for Advanced Electrocatalysis. *J. Am. Chem. Soc.* **2013**, *135*, 2013–2036.
(15) Bag, S.; Roy, K.; Gopinath, C. S.; Raj, C. R. Facile Single-Step Synthesis of Nitrogen-Doped Reduced Graphene Oxide-Mn_3O_4 Hybrid Functional Material for the Electrocatalytic Reduction of Oxygen. *ACS Appl. Mater. Interfaces* **2014**, *6*, 2692–2699.

(16) Guo, S.; Sun, S. FePt Nanoparticles Assembled on Graphene as Enhanced Catalyst for Oxygen Reduction Reaction. *J. Am. Chem. Soc.* **2012**, *134*, 2492−2495.
(17) Guo, S.; Zhang, S.; Wu, L.; Sun, S. Co/CoO Nanoparticles Assembled on Graphene for Electrochemical Reduction of Oxygen. *Angew. Chem., Int. Ed.* **2012**, *51*, 11770−11773.
(18) Wang, J. G.; Lv, Y. A.; Li, X. N.; Dong, M. D. Point-Defect Mediated Bonding of Pt Clusters on (5,5) Carbon Nanotubes. *J. Phys. Chem. C* **2009**, *113*, 890−893.
(19) Lv, Y. A.; Cui, Y. H.; Xiang, Y. Z.; Wang, J. G.; Li, X. N. Modulation of Bonding Between Noble Metal Monomers and CNTs by B-, N-doping. *Comput. Mater. Sci.* **2010**, *48*, 621−625.
(20) Xu, T. Y.; Zhang, Q. F.; Yang, H. F.; Li, X. N.; Wang, J. G. Role of Phenolic Groups in the Stabilization of Palladium Nanoparticles. *Ind. Eng. Chem. Res.* **2013**, *52*, 9783−9789.
(21) Zhong, X.; Yu, H.; Zhuang, G.; Li, Q.; Wang, X.; Zhu, Y.; Liu, L.; Li, X.; Dong, M.; Wang, J.-g. Pyridyne Cycloaddition of Graphene: "External" Active Sites for Oxygen Reduction Reaction. *J. Mater. Chem. A* **2014**, *2*, 897−901.
(22) Huang, X.; Neretina, S.; El-Sayed, M. A. Gold Nanorods: From Synthesis and Properties to Biological and Biomedical Applications. *Adv. Mater.* **2009**, *21*, 4880−4910.
(23) Vigderman, L.; Khanal, B. P.; Zubarev, E. R. Functional Gold Nanorods: Synthesis, Self-Assembly, and Sensing Applications. *Adv. Mater.* **2012**, *24*, 4811−4841.
(24) Chen, H.; Shao, L.; Li, Q.; Wang, J. Gold Nanorods and Their Plasmonic Properties. *Chem. Soc. Rev.* **2013**, *42*, 2679−2724.
(25) Yang, D. P.; Cui, D. X. Advances and Prospects of Gold Nanorods. *Chem.—Asian J.* **2008**, *3*, 2010−2022.
(26) Liu, L.; Ouyang, S.; Ye, J. Gold-Nanorod-Photosensitized Titanium Dioxide with Wide-Range Visible-Light Harvesting Based on Localized Surface Plasmon Resonance. *Angew. Chem., Int. Ed.* **2013**, *52*, 6689−6693.
(27) Fennell, J.; He, D.; Tanyi, A. M.; Logsdail, A. J.; Johnston, R. L.; Li, Z. Y.; Horswell, S. L. A Selective Blocking Method To Control the Overgrowth of Pt on Au Nanorods. *J. Am. Chem. Soc.* **2013**, *135*, 6554−6561.
(28) Wang, F.; Li, C.; Chen, H.; Jiang, R.; Sun, L. D.; Li, Q.; Wang, J.; Yu, J. C.; Yan, C. H. Plasmonic Harvesting of Light Energy for Suzuki Coupling Reactions. *J. Am. Chem. Soc.* **2013**, *135*, 5588−5601.
(29) Luo, J.; Njoki, P. N.; Lin, Y.; Wang, L.; Zhong, C. J. Activity-Composition Correlation of AuPt Alloy Nanoparticle Catalysts in Electrocatalytic Reduction of Oxygen. *Electrochem. Commun.* **2006**, *8*, 581−587.
(30) Zhang, J.; Sasaki, K.; Sutter, E.; Adzic, R. R. Stabilization of Platinum Oxygen-Reduction Electrocatalysts Using Gold Clusters. *Science* **2007**, *315*, 220−222.
(31) Zhao, D.; Xu, B.-Q. Enhancement of Pt Utilization in Electrocatalysts by Using Gold Nanoparticles. *Angew. Chem., Int. Ed.* **2006**, *45*, 4955−4959.
(32) Ye, X.; Jin, L.; Caglayan, H.; Chen, J.; Xing, G.; Zheng, C.; Doan-Nguyen, V.; Kang, Y.; Engheta, N.; Kagan, C. R.; Murray, C. B. Improved Size-Tunable Synthesis of Monodisperse Gold Nanorods Through the Use of Aromatic Additives. *ACS Nano* **2012**, *6*, 2804−2817.
(33) Grzelczak, M.; Pérez-Juste, J.; García de Abajo, F. J.; Liz-Marzán, L. M. Optical Properties of Platinum-Coated Gold Nanorods. *J. Phys. Chem. C* **2007**, *111*, 6183−6188.
(34) Grzelczak, M.; Perez-Juste, J.; Rodriguez-Gonzalez, B.; Liz-Marzan, L. M. Influence of Silver Ions on the Growth Mode of Platinum on Gold Nanorods. *J. Mater. Chem.* **2006**, *16*, 3946−3951.
(35) Nikoobakht, B.; El-Sayed, M. A. Preparation and Growth Mechanism of Gold Nanorods (NRs) Using Seed-Mediated Growth Method. *Chem. Mater.* **2003**, *15*, 1957−1962.
(36) Kresse, G.; Hafner, J. Ab-Initio Molecular-Dynamics for Open-Shell Transition-Metals. *Phys. Rev. B* **1993**, *48*, 13115−13118.
(37) Kresse, G.; Furthmuller, J. Efficient Iterative Schemes for Ab Initio Total-Energy Calculations Using a Plane-Wave Basis Set. *Phys. Rev. B* **1996**, *54*, 11169−11186.
(38) Kresse, G.; Joubert, D. From Ultrasoft Pseudopotentials to the Projector Augmented-Wave Method. *Phys. Rev. B* **1999**, *59*, 1758−1775.
(39) Norskov, J. K.; Rossmeisl, J.; Logadottir, A.; Lindqvist, L.; Kitchin, J. R.; Bligaard, T.; Jonsson, H. Origin of the Overpotential for Oxygen Reduction at a Fuel-Cell Cathode. *J. Phys. Chem. B* **2004**, *108*, 17886−17892.
(40) Zhang, S.; Shao, Y.; Liao, H.-g.; Liu, J.; Aksay, I. A.; Yin, G.; Lin, Y. Graphene Decorated with PtAu Alloy Nanoparticles: Facile Synthesis and Promising Application for Formic Acid Oxidation. *Chem. Mater.* **2011**, *23*, 1079−1081.
(41) Hu, Y.; Zhang, H.; Wu, P.; Zhang, H.; Zhou, B.; Cai, C. Bimetallic Pt-Au Nanocatalysts Electrochemically Deposited on Graphene and Their Electrocatalytic Characteristics Towards Oxygen Reduction and Methanol Oxidation. *Phys. Chem. Chem. Phys.* **2011**, *13*, 4083−4094.
(42) Yang, G.; Li, Y.; Rana, R. K.; Zhu, J.-J. Pt-Au/Nitrogen-Doped Graphene Nanocomposites for Enhanced Electrochemical Activities. *J. Mater. Chem. A* **2013**, *1*, 1754−1762.
(43) He, W.; Wu, X.; Liu, J.; Zhang, K.; Chu, W.; Feng, L.; Hu, X.; Zhou, W.; Xie, S. Pt-Guided Formation of Pt−Ag Alloy Nanoislands on Au Nanorods and Improved Methanol Electro-Oxidation. *J. Phys. Chem. C* **2009**, *113*, 10505−10510.
(44) Nilekar, A. U.; Mavrikakis, M. Improved Oxygen Reduction Reactivity of Platinum Monolayers on Transition Metal Surfaces. *Surf. Sci.* **2008**, *602*, L89−L94.
(45) Rao, C. V.; Cabrera, C. R.; Ishikawa, Y. Graphene-Supported Pt-Au Alloy Nanoparticles: A Highly Efficient Anode for Direct Formic Acid Fuel Cells. *J. Phys. Chem. C* **2011**, *115*, 21963−21970.
(46) Yu, L.; Pan, X.; Cao, X.; Hu, P.; Bao, X. Oxygen Reduction Reaction Mechanism on Nitrogen-Doped Graphene: A Density Functional Theory Study. *J. Catal.* **2011**, *282*, 183−190.
(47) Ikeda, T.; Boero, M.; Huang, S.-F.; Terakura, K.; Oshima, M.; Ozaki, J.-i. Carbon Alloy Catalysts: Active Sites for Oxygen Reduction Reaction. *J. Phys. Chem. C* **2008**, *112*, 14706−14709.
(48) Lim, D.-H.; Wilcox, J. Mechanisms of the Oxygen Reduction Reaction on Defective Graphene-Supported Pt Nanoparticles from First-Principles. *J. Phys. Chem. C* **2012**, *116*, 3653−3660.